

Torsional vibration signal analysis as a diagnostic tool for planetary gear fault detection

Song Xue, Ian Howard*

Department of Mechanical Engineering, Curtin University, Bentley, Western Australia, Australia
Department of Mechanical Engineering, Curtin University of Technology, GPO Box U1987, Perth,
WA 6845, Australia

* Corresponding author. Phone: (+61) 89266 7047.

E-mail: i.howard@curtin.edu.au

Abstract: This paper aims to investigate the effectiveness of using the torsional vibration signal as a diagnostic tool for planetary gearbox faults detection. The traditional approach for condition monitoring of the planetary gear uses a stationary transducer mounted on the ring gear casing to measure all the vibration data when the planet gears pass by with the rotation of the carrier arm. However, the time variant vibration transfer paths between the stationary transducer and the rotating planet gear modulate the resultant vibration spectra and make it complex. Torsional vibration signals are theoretically free from this modulation effect and therefore, it is expected to be much easier and more effective to diagnose planetary gear faults using the fault diagnostic information extracted from the torsional vibration.

In this paper, a 20 degree of freedom planetary gear lumped-parameter model was developed to obtain the gear dynamic response. In the model, the gear mesh stiffness variations are the main internal vibration generation mechanism and the finite element models were developed for calculation of the sun-planet and ring-planet gear mesh stiffnesses. Gear faults on different components were created in the finite element models to calculate the resultant gear mesh stiffnesses, which were incorporated into the planetary gear model later on to obtain the faulted vibration signal.

Some advanced signal processing techniques were utilized to analyse the fault diagnostic results from the torsional vibration. It was found that the planetary gear torsional vibration not only successfully detected the gear fault, but also had the potential to indicate the location of the gear fault. As a result, the planetary gear torsional vibration can be considered an effective alternative approach for planetary gear condition monitoring.

Keyword: Torsional vibration, Planetary gear fault diagnosis, Lumped-parameter model, Finite element model, Signal processing techniques

1. Introduction

Planetary gears, also known as epicyclic gear sets, commonly include several planet gears meshing simultaneously to split the torque and power. The planet gear can not only rotate around its own axis, but also around the planetary gear common axis. However, this rotating mechanism poses a big challenge for planetary gear condition monitoring compared to that of the parallel shaft gear. Additionally, the vibration level of the planetary gear system is also typically lower than the parallel shaft gear because of the self-centring capability of central members (sun gear, ring gear and the carrier) [1].

The traditional approach for condition monitoring of the planetary gear involves using a stationary transducer mounted on the ring gear casing to measure the vibration data when the planet gear passes by [2]. However, in this way, the measured vibration data exhibits a modulation effect caused by the carrier arm rotation. In the 1990s, a technique was developed for the time domain averages of the tooth meshing vibration of the individual planet gears and of the sun gear in an epicyclic gearbox [3-5]. Various window functions [5] could be used to capture the vibration data from the individual planet gear tooth as it was observed that the vibration level reached its peak when the corresponding planet gear was closest to the transducer [3]. Based on this, further signal processing techniques which have been used in the fixed axis gear could be used here to detect the gear fault. Moreover, numerous publications have also been focused on explaining the vibration spectrum caused by this carrier arm passing modulation [6-9] and it indicated that the sidebands would appear in the position of $f_m \pm n f_c$ ($n = 1, 2, 3, \dots$), with sideband spacing equal to the carrier arm rotation frequency f_c . McFadden and Smith pointed out that the asymmetry vibration spectra was caused by the fact that each planet gear had varying phase angles [6]. McNames applied Fourier series analysis to explain the source of the asymmetry observed in the spectrum and identified the location of the dominant frequency components near all harmonics of the meshing frequency [7]. Furthermore, Kahraman classified all the possible modulation sidebands into five different conditions based on the assembly condition and parameters of the planetary gear system [8]. Mark predicted additional sidebands in the frequency spectra produced by planet-carrier torque modulations, which might potentially mask the sidebands caused by damage in planetary gearboxes [2, 10]. Recently, Feng and Zuo summarised the planetary gear fault characteristics [11]. For the planetary gear system with a localized sun gear fault, the sidebands would appear in the position of $f_m \pm k f_s \pm n f_{sf} = f_m \pm k f_c \pm (k/N \pm n) f_{sf}$, with sideband spacing equals to the faulty sun gear rotational frequency f_{sf} . For the planetary gear system with a faulty planet gear, the sidebands would appear in the position of $f_m \pm k f_c \pm n f_{pf}$, with sideband spacing equals to the faulty planet gear rotation frequency f_{pf} . For the planetary system with a faulty ring gear, the sidebands would appear in the position of $f_m \pm n f_{rf}$, with sideband spacing equals to the faulty ring gear rotation frequency f_{rf} .

On the other hand, torsional vibration, measured from the gear shaft, also carries diagnostic information [12]. It would be an advantage to measure the torsional vibration directly to naturally separate the signal from the modulation effect. As a result, measuring the torsional vibration could be treated as an alternative way for condition monitoring of the planetary gear system. Limited publications on the planetary gear torsional vibration studies could be found. It was demonstrated by Wang in his thesis that the torsional vibration signal is far superior than the transverse signals for frequency analysis for all rotating components of planetary gearboxes [13]. Feng and Zuo gave explicit equations for the planetary gear torsional signal model indicating that the only modulation

effect in the torsional vibration signal was the amplitude and phase modulation caused by gear faults [14]. It was found that for the planetary gear system with a localized sun gear fault, the sidebands of the torsional vibration signal would appear in the position of $f_m \pm n f_{sf}^f$, with sideband spacing equals to the faulty sun gear rotational frequency f_{sf}^f . For the planetary gear system with a faulty planet gear, the sidebands of the torsional vibration signal would appear in the position of $f_m \pm n f_{pf}^f$, with sideband spacing equals to the faulty planet gear rotation frequency f_{pf}^f . For the planetary system with a faulty ring gear, the sidebands would appear in the position of $f_m \pm n f_{rf}^f$, with sideband spacing equals to the faulty ring gear rotation frequency f_{rf}^f . However, the big challenge of using this method is that there are so many faulty characteristic frequencies in the frequency spectrum and it becomes hard to determine which frequency component is the best choice. As a result, continuous research should be conducted on the analysis of the planetary gear torsional vibration.

Dynamic modelling of planetary gear vibration can be used to further the understanding of the vibration generation mechanisms in gear transmissions as well as the dynamic behaviour of the transmission in the presence of several types of gear faults. Kahraman presented a single-stage planetary gear train including the rigid body motions of the gears and the carrier arm to study the load sharing characteristics, the manufacturing error and the wear effect on the planetary gear dynamic response [15]. Lin and Parker further developed this model to including the gyroscopic effect to investigate a series of factors influencing the planetary gear natural frequency [16]. An extended three-dimensional model was developed by Velez to calculate the dynamic tooth loads on a planetary gear [17]. A planetary gear lumped parameter model considering the eccentricity error and planet position error was developed by Gu and the instantaneous gear geometry was used in the model [18, 19]. Chen incorporated the mesh stiffness of the internal gear pair with a crack into a 21DOF planetary gear model to investigate the dynamic response [20]. Based on a lump-parameter model, Liang investigated the vibration signal features of each component in the planetary gear system in the perfect and cracked situations [21].

The sun-planet and ring-planet tooth mesh stiffness variations and the resulting transmission errors were found to be the main internal vibration generation mechanisms for planetary gear systems. There were mainly analytical methods [20] and finite element (FE) methods to calculate the gear mesh stiffness [22-24]. The use of FE modelling was found to be most suitable for capturing the extended tooth contact phenomenon, especially when there was a crack at the gear tooth root, which could aggravate this effect [23]. Another issue was that the deviation between the gear mesh stiffness obtained from the analytical method and the FEA method was found to become larger with the increase in the crack size. The FE model was found to be more suitable for modelling the gear tooth mesh stiffness with larger gear tooth crack size [24].

Some advanced signal processing techniques could be used further to help in extracting the gear fault feature. The residual signal can be obtained by removing the regular gearmesh component and its harmonics while keeping the local variations. Initially, the residual signal was obtained from the frequency domain by removing the known gear mesh harmonics and then inverse Fourier transforming back to the time domain [25]. Narrowband envelope analysis was one of the prominent vibration signal processing techniques initially developed for the rolling bearing failure detection [26]. The idea behind this was that each time a localised defect in the gear makes contact under load with another surface it generated an extremely short duration impulse and its energy will be distributed across a very wide frequency range [26]. The amplitude modulation of the signal can be calculated by taking the absolute value of the signal's analytical signal and the phase modulation can be calculated by taking the phase of the

analytical signal [27-29]. McFadden analysed the amplitude modulation of the residual signal and it was found to be much more effective than using the time synchronous average (TSA) method alone [27]. Later on, McFadden also used the phase modulation of the residual TSA signal to detect fatigue cracks in the helicopter's main rotor gearbox [28]. Brie proposed an adaptive demodulation with an abrupt change detector. It was shown to have some superiority over the traditional demodulation process in some aspects [30]. Time-frequency analysis techniques were found to be very effective for conducting non-stationary signal analysis on vibration measurements to detect faults [31]. Some limitations were found when using the traditional time-frequency analysis technique, like the cross-terms and some improvement has been made to enhance the visual representation of the instantaneous frequency during the last decades. Most of these techniques were developed for the fault diagnosis for the fixed axis gear fault detection and it would be interesting to see the results if these techniques were used in the planetary gear fault diagnosis.

This paper aims to investigate the effectiveness of using the torsional vibration signal as a diagnostic tool for planetary gearbox fault detection. The original contribution of this paper compared with previous work is in utilizing the torsional vibration within one carrier arm to detect and distinguish the planetary gear faults. In section 2, a 20 degree of freedom planetary gear lumped-parameter model was developed and then in the following section, the finite element method was used to calculate the gear mesh stiffness. The original finite element planetary gear model has been developed in a previous paper. The sun-planet and ring-planet finite element models were created in this section and the faults in the sun gear, planet gear and ring gear were simulated in these models. The dynamic responses were obtained and studied using some common signal processing techniques in section 3 and then the potential advantages and limitations of this method were discussed in section 4.

2. The dynamic modelling of planetary gear system

2.1 Lumped-parameter modelling

Mathematical planetary gear models can be used to help understand the complex dynamic response from the gearbox [15] and the planetary gear system considered in this study was a single-stage planetary gear set, as shown in Fig. 1. The system consisted of an input motor, one sun gear, three planet gears, one ring gear, one carrier arm and an output load.

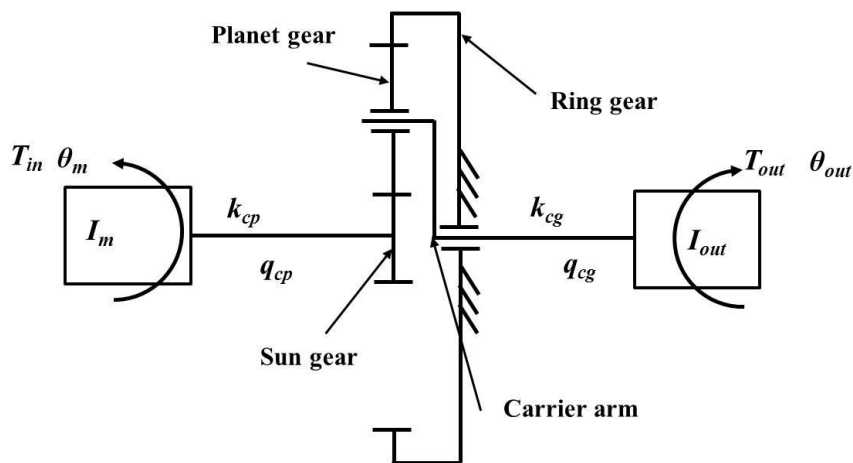


Figure 1 Planetary gear train model

A two-dimensional lumped-parameter planetary gear mathematical model was created to study the dynamic response and to obtain the dynamic mesh force in the gear system, as shown in Fig. 2. The subscript s represents the sun gear, r stands for the ring gear, c means carrier arm and $p1, p2, p3$ are the subscripts for the 1st, 2nd, 3rd planet gears respectively. Each of these components has three DOFs: transverse motions in the x -axis and y -axis, and rotation. The transverse motions of the sun, planet, ring and carrier ($x_j, y_j, j=s, r, c, p1, p2, p3$) were measured with respect to a rotating frame of reference fixed to the carrier [21].

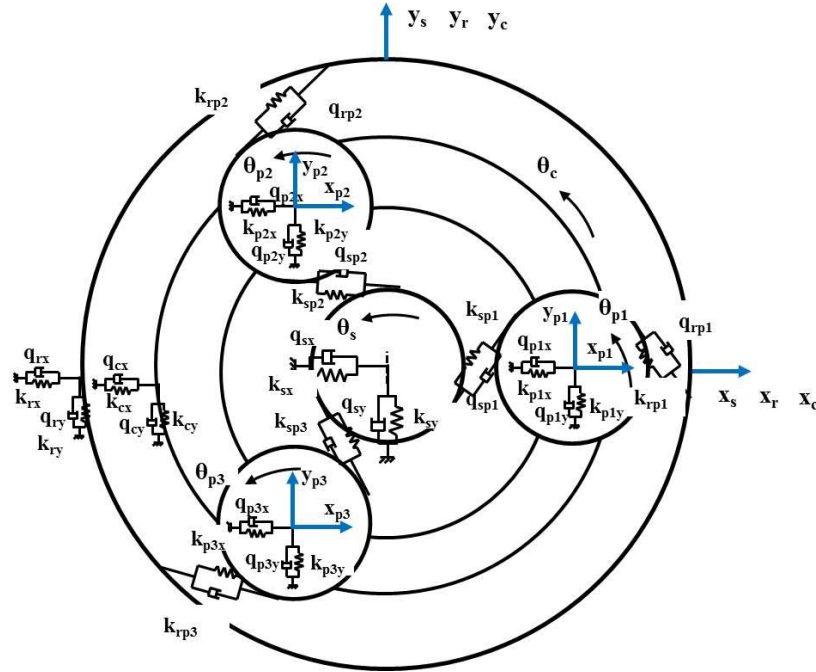


Figure 2 Lumped-parameter planetary gear model [21]

All the nomenclature used in this paper can be found in Appendix A. The resulting equations of motion for this planetary gear system can be found in appendix B. When designing the planetary gear system, the numbers of teeth on the sun gear and the ring gear must be chosen with their sum being a multiple of the number of planets. And here, to magnify the dynamic behaviour in the torsional direction, this paper used a very particular gear configuration, which was that the number of the planets was chosen to be 3 and both the sun gear and ring gear teeth numbers are a multiple of 3. The planetary gear parameters used in this paper are listed in table 1.

Table 1 Planetary gear parameters

	Sun gear	Planet gear	Ring gear
Number of teeth, Z_i	$Z_s=21$	$Z_p=39$	$Z_r=99$
Module, m_n	10 mm	10 mm	10 mm
Pressure angle, α_i	$\alpha_s=20^\circ$	$\alpha_p=20^\circ$	$\alpha_r=20^\circ$
Basic diameter, $d_{bi}=d_i \cos \alpha_i$	$d_{bs}=197$ mm	$d_{bp}=366$ mm	$d_{br}=930$ mm

Elastic Modulus, E	210MPa	210MPa	210MPa
Poisson's Ratio, ν	0.3	0.3	0.3

The bearing stiffness parameters are also chosen with some assumptions, as shown in appendix C. In the assumption, the sun gear stiffness was set to be 1×10^5 N/m, which is very low in comparison with others. The reason for this was because a floating sun gear is often desired in the practical planetary gear design to achieve an even load sharing in each planet gear [15]. In the simulation, this will lead to roughly only a global displacement of the sun gear.

2.2 Gear mesh stiffness calculation

Finite element (FE) modelling of gears with flexible contact provide more realistic simulations and to obtain quality converged solutions, adaptive meshing should be used so that the elements near the contact will have relatively small dimensions that enable the analysis to cope with the chaotic nonlinear nature of the contact region [33].

The tooth mesh stiffness variation of a sun-planet gear pair was modelled from the isolated sun-planet FE model, as shown in Fig. 3(a). The tooth mesh stiffness variation of a ring-planet gear pair was modelled from the isolated sun-planet FE model, as shown in Fig. 3(b). The detailed method on how to calculate these mesh stiffnesses was discussion in the previous paper [22, 34]. From the previous paper, the following facts about the gear mesh stiffness were known: (1). The major components in the mesh stiffness included the gear body stiffness, the teeth bending stiffness and the Hertzian contact stiffness; (2). the gear mesh stiffness value increased with the increase of the input loads; (3). there was a handover region between the double contact zone and the single contact zone and the length of the handover region will be slightly different with different input load; (4). in some extreme cases, the single contact zone could become triple contact zone as higher mesh forces were applied, which was due to the extended tooth contact phenomenon. In this paper, a constant input load was considered to minimise the impact from a varying input load on the gear mesh stiffness.

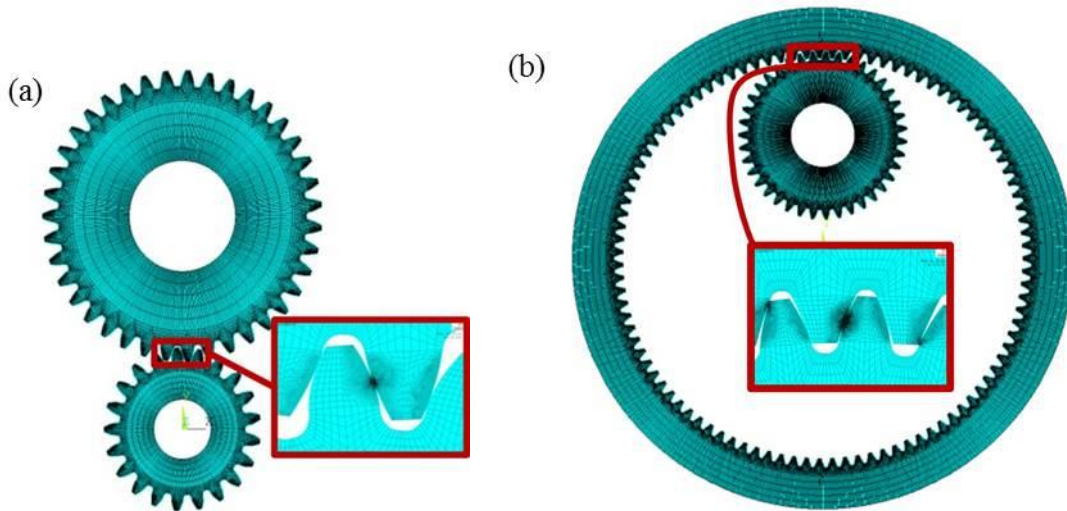


Figure 3 Finite element models, (a) isolated sun-planet external pair, (b) isolated ring-planet internal pair

The common gear failures include pitting, scuffing, wear, and root cracking [35]. Tooth root cracking is very uncommon but once it happens, it can result in catastrophic destruction of the gearbox. In this paper, a constant crack angle and constant crack length were assumed in both the external gear (sun gear and planet gear) and the internal gear (ring gear), as shown in Fig. 4. To use finite element methods to ascertain the changes in the teeth stiffness or transmission error with the existence of root cracks, the all-quad element meshing strategy is no longer possible due to the singularity near the crack front. Instead, triangular elements with their mid-side nodes located at $\frac{1}{4}$ of their adjacent edges from the crack tip will be used [36]. The LEFM (linear elastic fracture mechanics) assumption was used in this research.

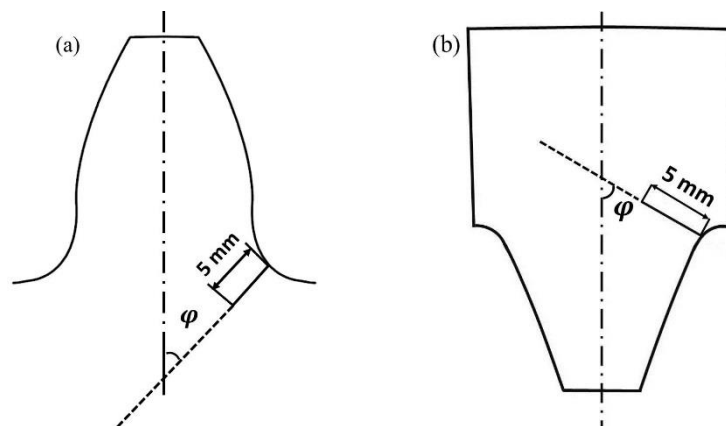


Figure 4 Gear crack example with crack angle $\varphi=60^\circ$ and crack length $l=5\text{mm}$, (a) external gear, (b) internal gear

Overall, there were four gear fault cases considered in this study. Case I involved a tooth crack in the sun gear and case II a tooth crack in a planet gear (sun side). Case III was a tooth crack in the planet gear (ring side) and case IV was a tooth crack in the ring gear. In some cases, the crack can affect each gear mesh stiffness in each branch, like the crack on the sun gear. All the information obtained here was based on the observations with respect to angular position of the fault impacts in each branch as well as over one carrier arm revolution. A summary of all the information can be found in table 2. In the table, K_{spi} ($i=1, 2, 3$) represents the sun-planet mesh

stiffness in the i th sun-planet mesh pair and K_{rpi} ($i = 1, 2, 3$) represents the ring-planet mesh stiffness in the i th ring-planet mesh pair. $\gamma s2$ and $\gamma s3$ are the gear mesh phase between the 1st sun-planet pair and the 2nd sun-planet pair as well as the 3rd sun-planet pair respectively. According to the planetary gear parameters in table 1, all the mesh phases were calculated as 0° in this paper. θ_m is the carrier arm rotation angle covering one gear tooth and is equal to $360^\circ/Z_r$ (3.6°). In case I, all the sun-planet mesh stiffness curves were affected. If the position of the fault in K_{sp1} was at 0° , the positions of the fault in K_{sp2} and K_{sp3} were at $(7+\gamma s2)\theta_m$ and $(14+\gamma s3)\theta_m$ respectively. The total number of fault impacts in one carrier arm revolution was observed to be 14 and their fault interval was $(7+\gamma s2)\theta_m$. $\gamma s2$, $\gamma s3$ are the gear mesh phase between the 1st sun-planet pair and the 2nd sun-planet pair and 3rd sun-planet pair separately [37]. They were calculated as 0 according to the parameters in table 1 as well, which meant the three sun-planet pairs were all in phase. $\gamma r2$, $\gamma r3$ are the gear mesh phase between the 1st ring-planet pair and the 2nd ring-planet pair and 3rd ring-planet pair separately [37]. In case II, only one sun-planet mesh stiffness curve was affected and the total number of faults in one carrier arm was 3. The fault interval in this case was $39\theta_m$. Similarly, only one ring-planet curve in case III was affected by the fault and the total number of faults over one carrier arm was 3. The fault interval in this case was also $39\theta_m$. In case IV, all the ring-planet mesh stiffness curves were affected and the total number of fault impacts in one carrier arm revolution was 3. The fault interval here was $33\theta_m$.

Table 2 Summary of the observation in the sun-planet and ring-planet mesh stiffnesses

	Shaft rotation in each branch			One carrier arm revolution	
	Curve	Fault impact or not	Position of the fault impact	Number of fault impacts in total	Faults interval
Case I	K_{sp1}	Yes	0°	14	$(7+\gamma s2)\theta_m = 25.5^\circ$
	K_{sp2}	Yes	$(7+\gamma s2)\theta_m = 25.5^\circ$		
	K_{sp3}	Yes	$(14+\gamma s3)\theta_m = 51^\circ$		
	K_{rpi} ($i = 1, 2, 3$) remains unaffected in this case.				
Case II	K_{sp1}	Yes	0°	3	$39\theta_m = 141.8^\circ$
	K_{sp2}	No	—		
	K_{sp3}	No	—		
	K_{rpi} ($i = 1, 2, 3$) remains unaffected in this case.				
Case III	K_{rp1}	Yes	0°	3	$39\theta_m = 141.8^\circ$
	K_{rp2}	No	—		
	K_{rp3}	No	—		
	K_{spi} ($i = 1, 2, 3$) remains unaffected in this case.				
Case IV	K_{rp1}	Yes	0°	3	$33\theta_m = 120^\circ$
	K_{rp2}	Yes	$(33+\gamma r2)\theta_m = 120^\circ$		
	K_{rp3}	Yes	$(66+\gamma r3)\theta_m = 240^\circ$		
	K_{spi} ($i = 1, 2, 3$) remains unaffected in this case.				

Case III has been plotted as one example of the results. If the planet gear has a crack on the ring gear side, only one pair of the ring-planet gears will be affected by the planet tooth crack. However, the sun-planet mesh stiffness

can be assumed to not be affected as the cracked planet tooth can still bear the compressive stiffness from the sun-planet mesh as if no crack exists [38]. Fig. 5 shows the three ring-planet gear mesh stiffnesses with the effect of the crack on the 1st ring-planet mesh pair. In the figure, one full planet gear shaft rotation was considered, which corresponded to 141.8 degrees of carrier arm rotation. Fig. 6 described the variation of the ring-planet mesh stiffness curve K_{rp1} for one carrier arm rotation.

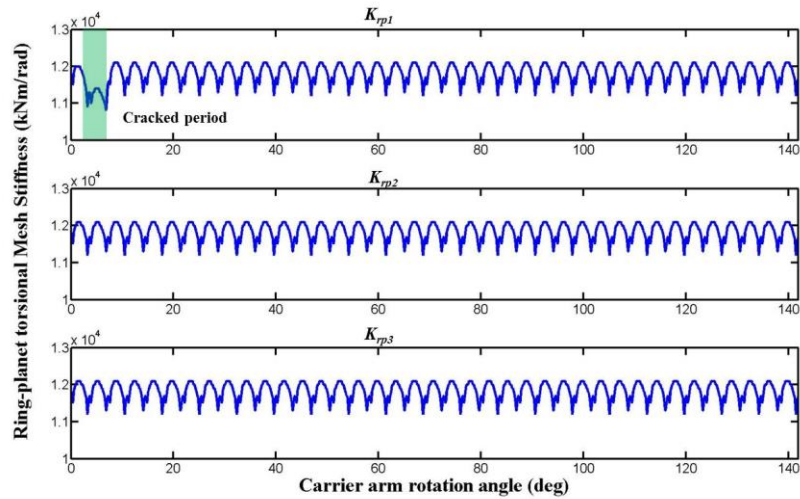


Figure 5 Ring-planet mesh stiffness with crack on the 1st ring-planet mesh pair

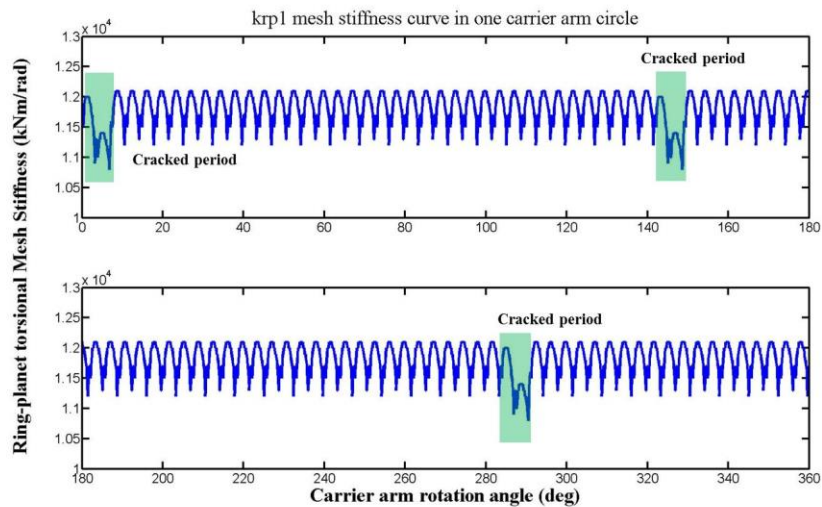


Figure 6 Mesh stiffness of the 1st planet-ring over one carrier arm revolution

2.3 Gear vibration spectrum characteristic

When analysing the vibration spectrum of the planetary gear, the first property of interest in a planetary gear system is the tooth meshing frequency, f_m . In this research, the ring gear is stationary and the sun gear, planet gear and the carrier arm rotate with respect to their own axes. Under this case, the tooth mesh frequency of the planetary gear can be calculated as [3],

$$f_m = Z_r f_c, \quad (1)$$

where f_c is the carrier arm rotational frequency. As the frequency spectra is expressed in terms of the carrier arm shaft order, the meshing frequency component should appear in the position of Z_r in this paper. For the local sun gear damage case, in one relative rotation cycle with respect to the carrier arm, the characteristic fault rotational frequency is given by [11, 14],

$$f_{sf}^c = N \frac{f_m}{Z_s} = N \frac{Z_r}{Z_s} f_c, \quad (2)$$

where f_{sf} is the faulty sun gear rotation frequency with respect to the carrier arm. N is the number of planet gears in the system. Similarly, for the local planet gear damage case, in one relative rotation cycle with respect to the carrier arm, the characteristic fault rotational frequency is given by [11, 14],

$$f_{pf}^c = \frac{f_m}{Z_p} = \frac{Z_r}{Z_p} f_c, \quad (3)$$

where f_{pf} is the faulty planet gear rotation frequency with respect to the carrier arm. For the local ring gear damage case, in one relative rotation cycle with respect to the carrier arm, the characteristic fault rotational frequency is given by [11, 14],

$$f_{rf}^c = N \frac{f_m}{Z_r} = N f_c, \quad (4)$$

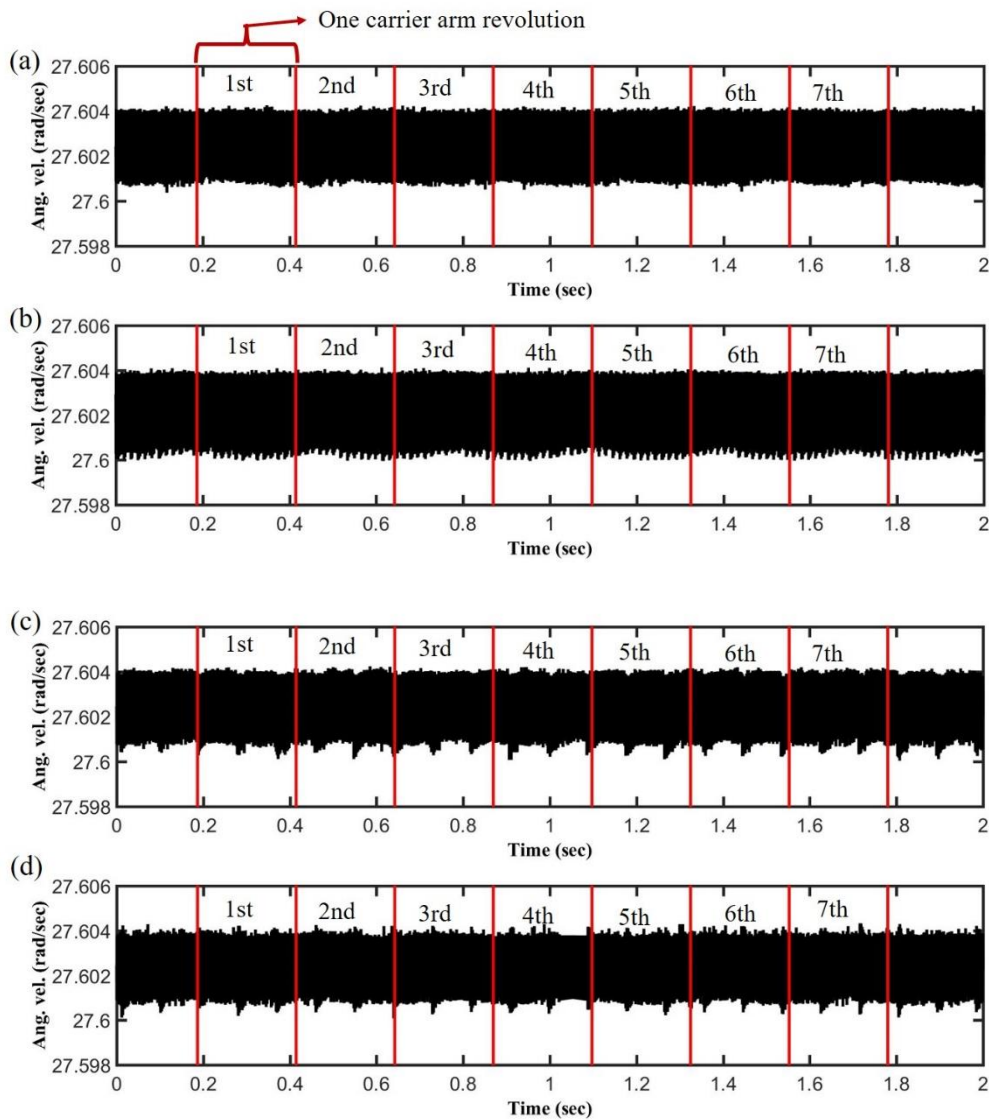
where f_{rf} is the faulty ring gear rotation frequency with respect to the carrier arm.

3. Numerical simulation and result analysis

Instantaneous angular speed (IAS) has been emerging in the condition monitoring and diagnosis of rotating machines, such as bearings, gears, synchronous belts, etc [39-41]. The IAS signals can be naturally sampled in the angular domain and shows greater sensitivity to different types of defects in the machine over a large bandwidth of orders [42]. The instantaneous carrier arm angular velocity in the planetary gear has been selected to diagnosis the gear faults in this research. In addition, the carrier arm angular velocity was also naturally free from the modulation effect caused by the transfer path and it was also demonstrated by Zhongwei in his thesis that the torsional vibration signal is far superior than the transverse signals for frequency analysis for all rotating components of planetary gearboxes [13]. Some common diagnostic algorithms can be used to analysis the fault result, such as the RMS spectrum, residual signal, narrow band envelope, and amplitude and phase demodulation, and time-frequency analysis.

The MATLAB ode solver was used to solve the planetary gear differential equations and a constant input load was applied to the input motor, which was $T_{in}=100\text{Nm}$. The output load $T_{out}=0.75 \times \dot{\theta}_{out}^2$ was applied to the output load and it was assumed to depend on the carrier arm angular velocity. The coefficient 0.75 was used to describe the characteristics of the output load. Numerical simulations were performed using the OED solver in Matlab and the chosen integration time intervals was 0.0001s. After the initial transient start-up phase has decayed away and the steady-state conditions were obtained, the system was simulated over several seconds. The presence of the crack can introduce some transient disturbance into the gear system, even though the gear system is still in the

steady-state vibration stage. After the simulation has been obtained, the relevant degree of freedom data was transformed from the time domain to the phase domain for each shaft of interest. This required interpolation to ensure an exact integer number of points per shaft rotation, using a cubic spline fit for the varying shaft speed, for each shaft of interest. Both the healthy and faulty mesh stiffnesses can be interpolated based on the curves obtained in Section 2. The angular positions of the sun gear, planet gear and the carrier arm were kept separately and all the cracked zones were assumed before the simulation. When it entered the cracked zones, the computer program can automatically interpolate the value from the faulty mesh stiffnesses. Fig. 7 shows the carrier arm angular velocity signal over 2 seconds, which included 7 carrier arm revolutions or 40 sun gear revolutions. This is because the total gear ratio is given by Z_s over (Z_s+Z_r) or $7/40$. There are five plots shown in the figure, corresponding to the condition of the healthy planetary gear, planetary gear with cracked sun gear, planetary gear with cracked planet gear on the sun gear side, planetary gear with cracked planet gear on ring gear side as well as planetary gear with cracked ring gear separately.



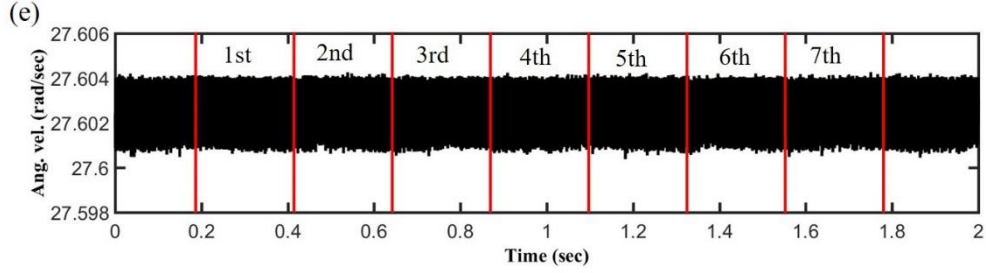


Figure 7 Carrier arm angular velocity over 2 seconds. (a) healthy planetary gear case; (b) planetary gear with cracked sun gear case; (c) planetary gear with cracked planet gear on the sun gear side case; (d) planetary gear with cracked planet gear on the ring gear side case; (e) planetary gear with cracked ring gear case.

Fig. 8 shows the results of the RMS spectra from the carrier arm angular velocity where the x-axis has been presented in terms of carrier arm orders or shaft order. The first observation from the figure is that the RMS spectra have gear mesh components at order 99 and its harmonics, like 198, 297 and so on. This observation has been consistent with the analysis in [14], where the mesh frequency is the carrier arm frequency times the ring gear tooth number. A closer look at these mesh components can be made to check the amplitude of the mesh component and the second harmonic was chosen here. The amplitude for the healthy case was around -33.20 dB and the amplitude for the other four cases were very similar at levels of -33.99 dB, -33.19 dB, -33.20 dB, and -33.24 dB respectively. As discussed previously, the faults on different components have their own characteristic frequency and their positions can be identified. The amplitude on these positions could also be used for fault diagnostics. For the planetary gear with the sun gear fault, the position of the sun gear characteristic frequency in Fig. 8 (b) is $k \cdot Z_r \pm n \cdot N \cdot (Z_r/Z_s)$ [14]. For example, the amplitude of the frequency component at position 170 (for the case of $2 \times 99 - 2 \times 3 \times 99/21$) could be checked and it was found to be -55.54 dB compared with the value of -65.04 dB in the healthy condition. The amplitude of the frequency component at position 184 (for the case of $2 \times 99 - 1 \times 3 \times 99/21$) could be checked and it was found to be -62.43 dB compared with the value of -61.75 dB in the healthy condition. The amplitude of the frequency component at position 212 (for the case of $2 \times 99 + 1 \times 3 \times 99/21$) could be checked and it was found to be -53.09 dB compared with the value of -61.79 dB in the healthy condition. There are numerous options here, like the components in the position 14, 28, 42, 57 and so on. For the planetary gear with the planet gear fault, the position of the planet gear characteristic frequency in Fig. 8 (c) is $k \cdot Z_r \pm n \cdot (Z_r/Z_p)$ [14]. For example, the amplitude of the frequency component at position 201 (for the case of $2 \times 99 + 1 \times 99/39$) could be checked and it was found to be -55.28 dB compared with the value of -54.87 dB in the healthy conditions. The same position in Fig. 8 (d) could be checked and the amplitude was found to be -55.23 dB compared with the value of -54.87 dB in the healthy condition. The differences in these two cases were not as significant as the one in the faulty sun gear case. For the planetary gear with the ring gear fault, the position of the ring gear characteristic frequency in Fig. 8 (e) is $k \cdot Z_r \pm n \cdot N$ [14]. For example, the amplitude of the frequency component at position 201 (for the case of $2 \times 99 + 3$) could be checked and it was found to be -56.17 dB compared with the value of -54.87 dB in the healthy condition. The big challenge of comparing the frequency spectra is that there are so many faulty characteristic frequencies and it becomes hard to determine which frequency component is the best choice.

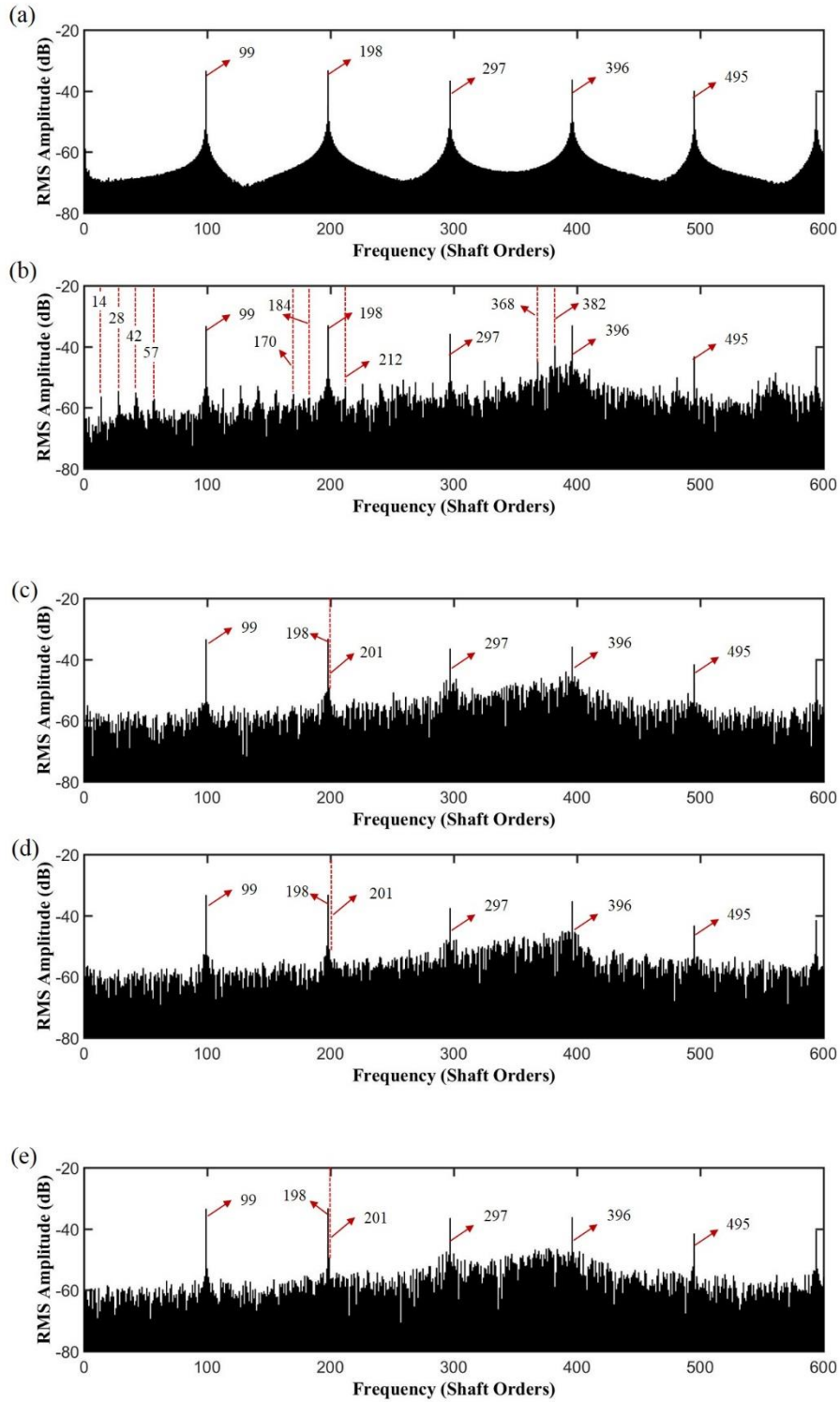


Figure 8 RMS spectrum amplitude results. (a) healthy planetary gear case; (b) planetary gear with cracked sun gear case; (c) planetary gear with cracked planet gear on the sun gear side case; (d) planetary gear with cracked planet gear on the ring gear side case; (e) planetary gear with cracked ring gear case.

It should be noticed that within one carrier arm revolution, all the gear teeth, no matter if it is the sun gear tooth or the ring gear tooth, will get in contact at least once, which means all the information from the gear teeth can be obtained within one carrier arm revolution. If the carrier arm enters the next revolution, all the same teeth mesh

information will still be contained in this revolution but the order of the teeth engagement will be different. As a result, the proposed diagnostic method examines the gear information within one carrier arm rather than the information over several seconds. For the subsequent data analysis, data files were created for storing the simulation results, including the sample times for each data point. This necessitated the manipulation of the data from variable time step form to equispaced phase form. The resampling of the original data into equispaced phase data was accomplished using 65536 (2^{16}) points per carrier arm revolution to eliminate any possibility of aliasing [43]. Exactly one revolution of resampled data was used for subsequent analysis.

Fig. 9 shows the results of the carrier arm angular velocity signal, which has been resampled into equi-spaced phase data over one carrier arm revolution. As shown in Fig. 9, the presence of the crack on different components can be identified by visually looking at these waveforms as several repetitive impacts on the carrier arm torsional velocity curves can be observed. The impacts are caused by the mesh stiffness reduction due to the crack and the number of these impacts corresponds to the number of the cracked periods within one carrier arm revolution. A closer look at the simulation results can be achieved by using some statistical indicators, which have been summarized in table 3.

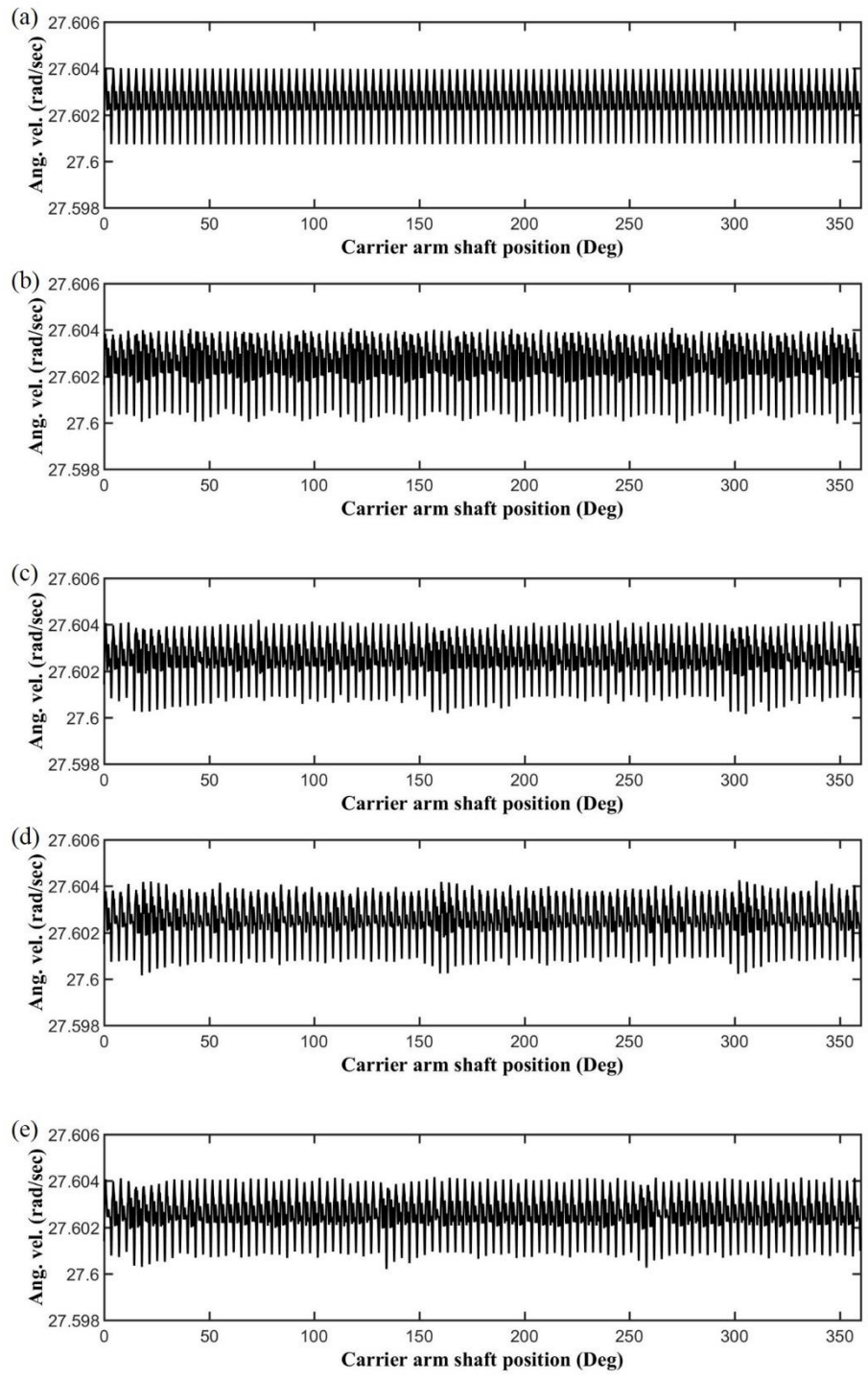


Figure 9 Carrier arm angular velocity over one carrier arm revolution. (a) healthy planetary gear case; (b) planetary gear with cracked sun gear case; (c) planetary gear with cracked planet gear on the sun gear side case; (d) planetary gear with cracked planet gear on the ring gear side case; (e) planetary gear with cracked ring gear case.

Table 3 Comparison of the statistical indicators of the diagnostic results

	Healthy	Cracked sun gear	Cracked planet gear sun gear side	Cracked planet gear ring gear side	Cracked ring gear
Mean	27.6026	27.6026	27.6026	27.6026	27.6026
STD	7.54×10^{-4}	9.12×10^{-4}	7.74×10^{-4}	7.75×10^{-4}	7.58×10^{-4}
Skew	-0.447	-0.833	-0.498	-0.447	-0.402
Kurtosis	3.15	3.28	3.19	3.01	3.08
Crest Factor	4.36	4.69	5.21	5.62	5.23

The advanced diagnostic algorithms which are commonly used for gearbox vibration analysis were used on the simulation results. These algorithms include residual signal, narrow band envelope using different mesh harmonics, and amplitude and phase demodulation using different mesh harmonics. The analysis of the diagnostic parameter kurtosis is given in table 4 for all the waveforms with and without the tooth crack. As shown in the table, the most effective diagnostic algorithms were the residual signal kurtosis, envelope kurtosis using the 4th mesh harmonic as well as the amplitude modulation using the 4th mesh harmonic. Some differences between the faulty case and the healthy case can still be observed in the other algorithms, but not as obviously compared to those shown here.

Table 4 Analysis of the diagnostic parameter kurtosis for all cases

		Healthy	Cracked sun gear	Cracked planet gear sun gear side	Cracked planet gear ring gear side	Cracked ring gear
Residual signal kurtosis		2.81	5.47	3.58	4.84	3.84
Envelope kurtosis	2 nd mesh harmonic	1.97	3.77	2.90	3.76	3.42
	4 th mesh harmonic	2.85	3.58	4.98	8.78	5.37
Amplitude modulation kurtosis	2 nd mesh harmonic	1.81	2.79	3.29	2.84	2.33
	4 th mesh harmonic	1.90	2.09	5.44	7.65	6.65
Phase modulation kurtosis	2 nd mesh harmonic	1.86	2.89	2.63	2.80	2.82
	4 th mesh harmonic	1.77	2.60	2.23	2.67	2.23

Fig. 10 shows the results of the residual signal and the presence of the crack on different components can be noted. The residual signal significantly enhances the detectability of the gear fault in the signal and some abnormal signals can be easily found in the wave form. The kurtosis for all the cases, from the healthy case to the cracked ring gear case, are 2.81, 5.47, 3.58, 4.84, and 3.84 respectively as outlined in Table 4.

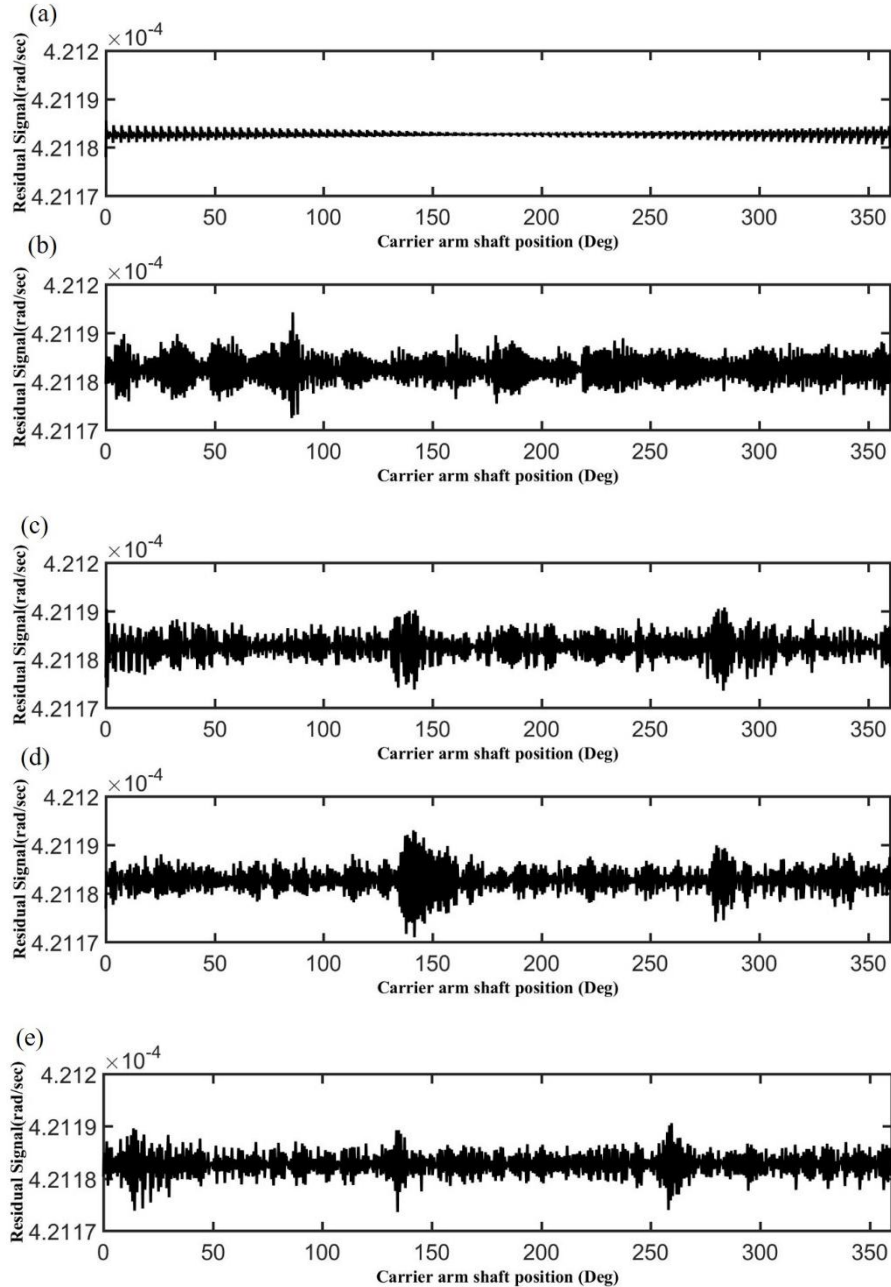


Figure 10 Residual signal results. (a) healthy planetary gear case; (b) planetary gear with cracked sun gear case; (c) planetary gear with cracked planet gear on the sun gear side case; (d) planetary gear with cracked planet gear on the ring gear side case; (e) planetary gear with cracked ring gear case.

The narrow band envelope analysis has been developed in the early 1970's and has become one of the prominent vibration signal processing techniques for detection and diagnosis of the incipient mechanical failure [44]. The second and the fourth mesh harmonic was chosen for the demodulation process and a bandwidth of 98 shaft orders (± 49) was used for the analysis. As indicated in table 3, the results from the fourth mesh harmonic appeared to be

more obvious than the results from the second mesh harmonic. Fig. 11 shows the results of the narrow band envelope using the fourth mesh harmonic for the healthy gear case, cracked sun gear case, cracked planet gear cases on both its mesh sides and cracked ring gear cases. The red line is the result for the healthy gear case and it is compared with the other faulty gear cases in Fig. 11 (b)–(e). The visual impression from the figures reveals the presence of the crack on the sun gear and the planet gear on the sun gear side with different variation patterns. The healthy gear case results were compared with the faulty gear cases in Fig. 11(b)–Fig. 11(e). For example, compared with the healthy gear case, there were fourteen fault impulses within one carrier arm rotation when the crack occurs on the sun gear and they have equal space between each other as shown in Fig. 11 (b). In Fig. 11(c), three obvious impulses could be observed at the position of around 20-deg, 160-deg and 300-deg. The same scenario could also be observed in Fig. 11(d). In Fig. 11(e), three obvious impulses are found in the position of 20-deg, 140-deg and 260-deg compared with the healthy gear case. Even though both the results from the faulty planet gear and faulty ring gear include three impulses, it is important to mention here that the space between the impulses is not equal. The impulse space in the faulty planet gear is around 140-deg while the impulse space in the faulty ring gear is around 120-deg.

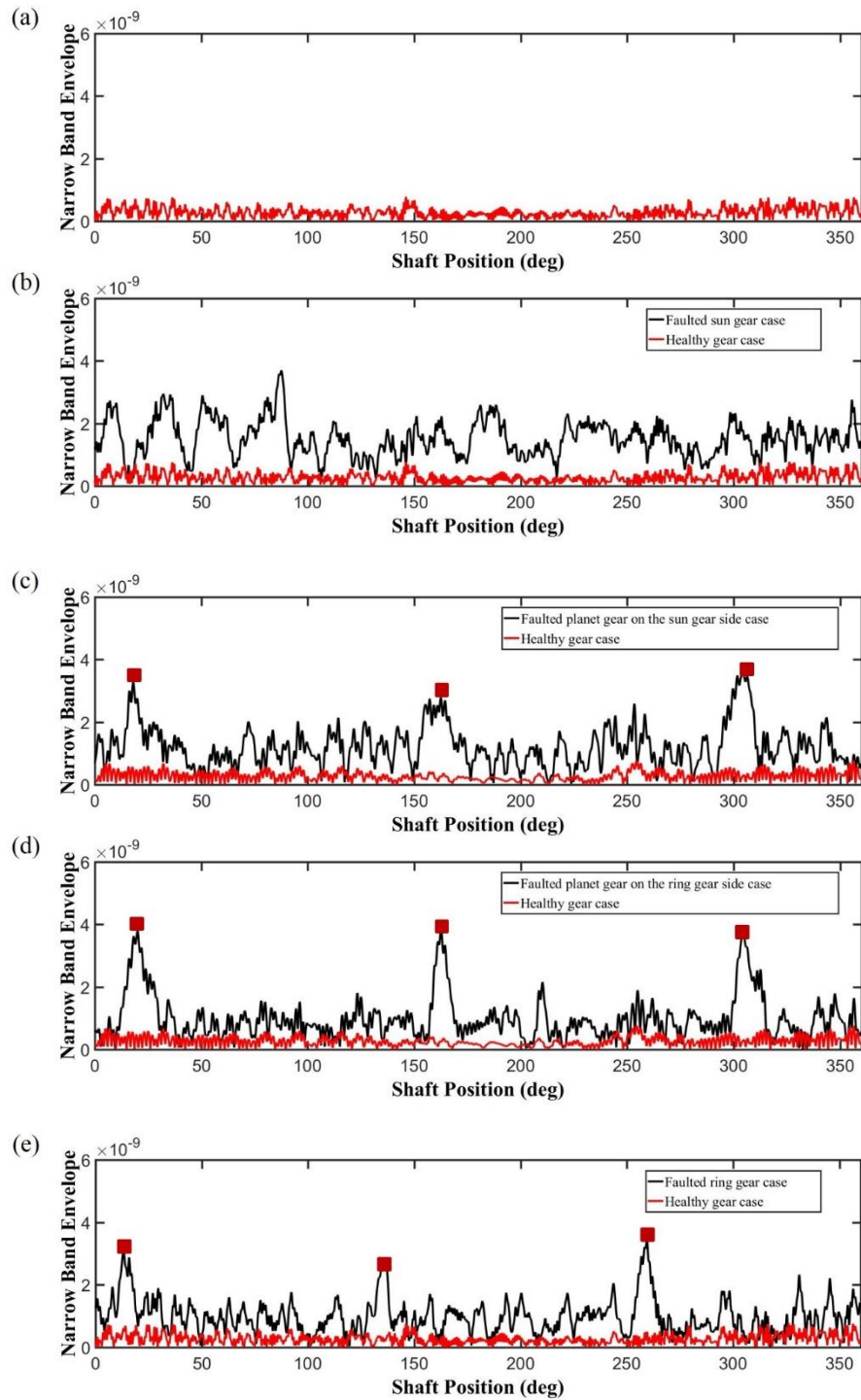


Figure 11 Narrowband envelope results using the fourth mesh harmonic. (a) healthy planetary gear case; (b) planetary gear with cracked sun gear case; (c) planetary gear with cracked planet gear on the sun gear side case; (d) planetary gear with cracked planet gear on the ring gear side case; (e) planetary gear with cracked ring gear case.

Another effective technique to detect the cracks indicated by table 3 is amplitude demodulation of the vibration signal using the fourth mesh harmonic and it can be described in terms of the Hilbert transform and the analytic signal. The amplitude of the analytic signal represents the amplitude modulation and the phase of the analytic

signal represents the phase modulation. The bandwidth of 98 shaft orders (± 49) was used for the analysis. Fig. 12 shows the results of the amplitude modulation and phase modulation using the fourth mesh harmonic from the carrier arm angular velocity. The left column shows the results of the amplitude modulation and the right column shows the results of the phase modulation. The healthy gear case results were compared with the faulty gear cases in Fig. 12(b)–Fig. 12(e). Similarly, the visual impression from the figures can reveal the presence of the crack. For example, the amplitude demodulation and phase demodulation in Fig. 12(b) clearly reflects the presence of the crack on the sun gear as the fault impulses are visible and the fault impulse number is clear, which is 14. The overall phase modulation undergoes a reduction of 30-deg and the impulses in the phase modulation are also visible. The fault perturbations in the planet gear and ring gear are also visible in the amplitude modulation results. However, the fault perturbations in the phase modulation results were buried by the large variations, which makes the fault impulses harder to identify.

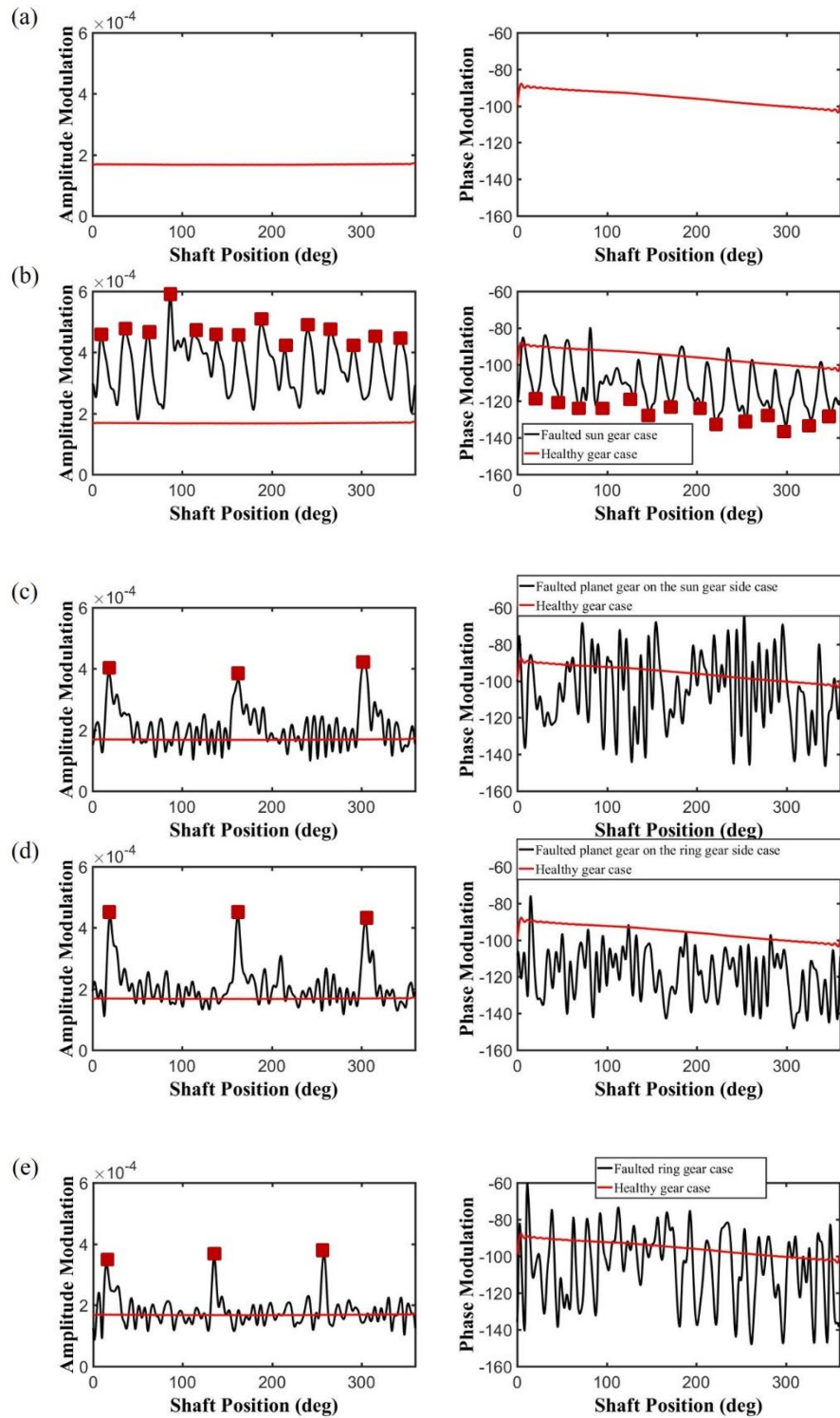


Figure 12 Amplitude demodulation and phase demodulation results using the fourth mesh harmonic. (a) healthy planetary gear case; (b) planetary gear with cracked sun gear case; (c) planetary gear with cracked planet gear on the sun gear side case; (d) planetary gear with cracked planet gear on the ring gear side case; (e) planetary gear with cracked ring gear case.

The Wigner-Ville distribution (WVD) is one of the well know time-frequency analysis methods and its application to the detection of the gear damage has been widely described recently. However, the cross-terms in the WVD have limited its application and by applying a suitable window function in the time domain, the so-called pseudo Wigner-Ville distribution (PWVD) can be obtained, which can attenuate the cross-terms. Fig. 13 shows the PWVD of the carrier arm angular velocity residual signal. As shown in the figure, the residual signal instead of the original signal was used here because removing the components at the meshing harmonics can increase the sensitivity to energy changes related to the gear damage and a much clearer energy distribution pattern can be observed in the figure. Compared with the healthy case in Fig. 13(a), the energy distribution related to the damage can be observed in Fig. 13(b), Fig. 13(c), Fig. 13(d) and Fig. 13(e), corresponding to the sun gear damage, the planet gear damage (both sun gear side and ring gear side) and ring gear damage respectively. If the crack occurred on the sun gear, the PWVD pattern tends to show a uniform distribution along its mesh component. This is largely because the sun gear crack repeats itself 14 times within one carrier arm rotation and these impacts are occurring uniformly during the rotation. Similarly, if the crack occurred on the planet gear, the PWVD energy patterns tend to be concentrated on three positions, corresponding to the moment when the cracked tooth was in contact, as shown in Fig. 13(c) and Fig. 13(d). If the crack occurred on the ring gear, the PWVD energy also tends to be concentrated on three positions. However, it is interesting to note that the faulty ring gear PWVD energy seems to concentrate in a smaller range compared with the faulty planet gear result, as shown in Fig. 13(e).

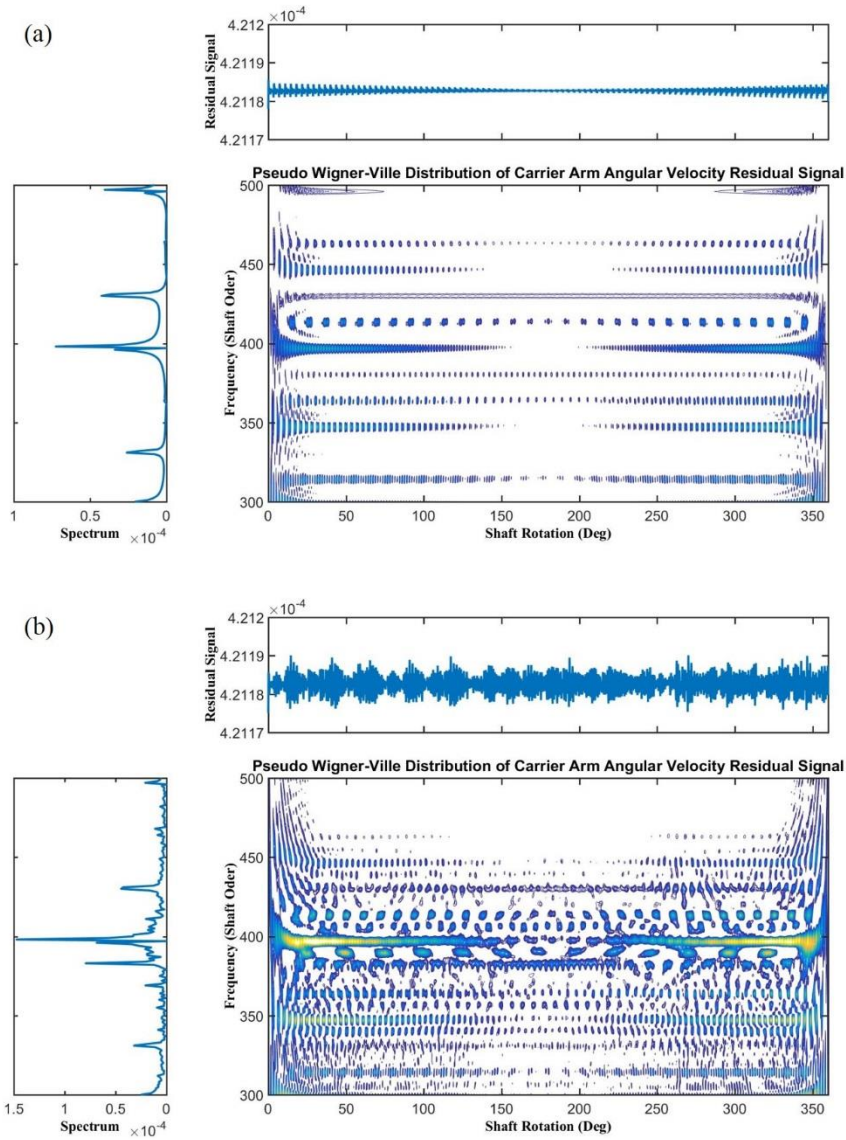


Figure 13 Pseudo Wigner–Ville distribution (PWVD) of the carrier arm angular velocity residual results. (a) healthy planetary gear case; (b) planetary gear with cracked sun gear case; (c) planetary gear with cracked planet gear on the sun gear side case; (d) planetary gear with cracked planet gear on the ring gear side case; (e) planetary gear with cracked ring gear case.

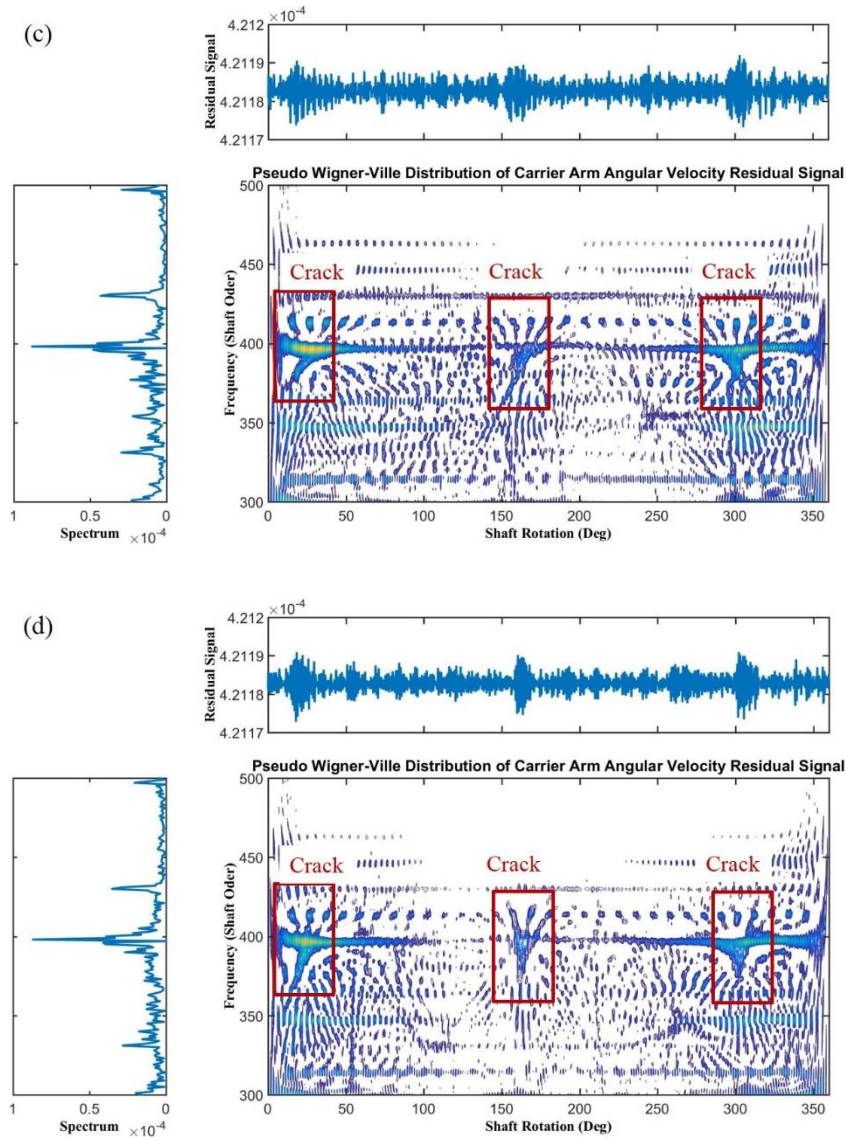


Figure 13 (continued) Pseudo Wigner–Ville distribution (PWVD) of the carrier arm angular velocity residual results. (a) healthy planetary gear case; (b) planetary gear with cracked sun gear case; (c) planetary gear with cracked planet gear on the sun gear side case; (d) planetary gear with cracked planet gear on the ring gear side case; (e) planetary gear with cracked ring gear case.

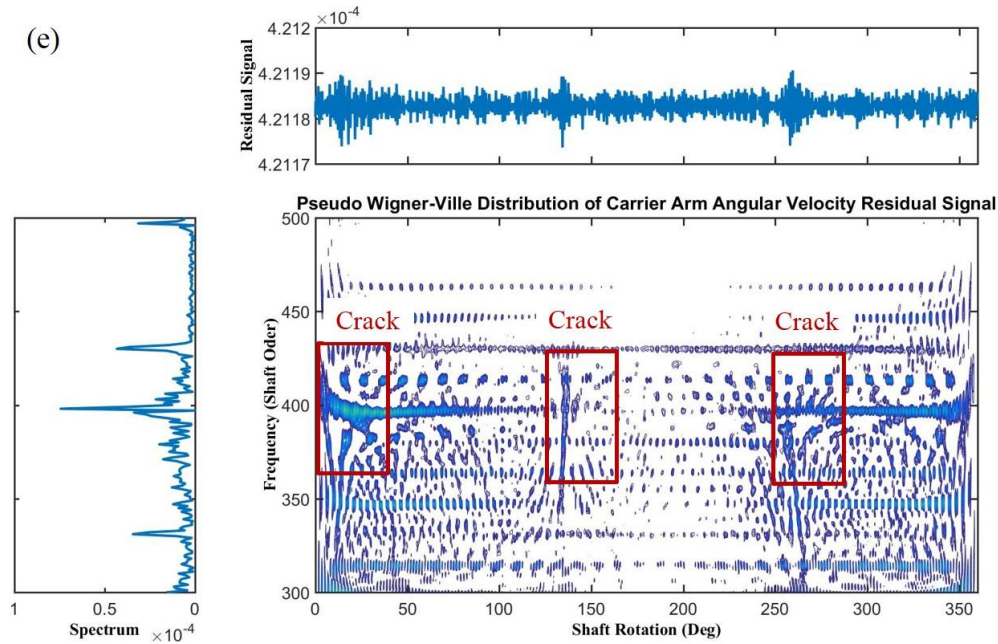


Figure 13 (continued) Pseudo Wigner–Ville distribution (PWVD) of the carrier arm angular velocity residual results. (a) healthy planetary gear case; (b) planetary gear with cracked sun gear case; (c) planetary gear with cracked planet gear on the sun gear side case; (d) planetary gear with cracked planet gear on the ring gear side case; (e) planetary gear with cracked ring gear case.

4. Discussion

This paper has discussed the effectiveness of using the planetary gear torsional vibration to detect the gear faults as the torsional vibration was found to be free from the modulation caused by the carrier arm passing effect [14]. Lumped-parameter modelling was used in this paper to generate the faulted gear dynamic response and there were several major assumptions in the theoretical model itself, like the gear only vibrated in the 2-dimensional plane, the friction forces between the teeth were ignored, the geometrical and profile errors were neglected and the backlash was also ignored. The account of any of these effects would change the resulting gear dynamic response presented here, as has been demonstrated by the other authors [45]. Another major assumption in this model is that the LEFM (linear elastic fracture mechanics) assumption was used when modelling the gear crack using the finite element method. Some researches indicate that the profile errors due to plastic deformation could have a significant effect on the possibility of detecting a gear tooth crack [46]. However, the LEFM was used in this paper and the plastic deformation effect will be studied in the future. The purpose of all these assumptions is to ensure that the spectra of the desired torsional vibration is relatively clear and only contains the impact from the gear faults. In this way, it is easier to analyse the effectiveness of using the planetary gear torsional vibration to detect the gear fault.

There are several options when choosing the torsional vibration in the planetary gear. The sun gear torsional vibration or the planet gear torsional vibration or even the ring gear torsional vibration can also be considered to

analyse the faulted gear dynamics. The reason for choosing the carrier arm angular velocity in this research is because within one carrier arm revolution, all the gear teeth, no matter if it is the sun gear tooth or the ring gear tooth, will be in contact at least once, which means all the information from the gear teeth can be obtained within one carrier arm revolution. In the traditional separation method with the stationary transducer on the ring gear [2, 3, 4, 10], capturing of all the information from the sun gear or the planet gear needs multiple carrier arm revolutions to finish and then be reassembled in the right order. In other words, if the number of the sun gear teeth is N_s in a planetary gear system, it needs at least N_s carrier arm revolutions to record all the sun gear information. The choosing of the carrier arm torsional vibration not only ensures the integrity of the information from the sun gear, but also enhances the efficiency of recording the vibration.

Initially, the total simulations were recorded over several seconds covering more than 7 carrier arm revolutions. This is because the total gear ratio is given by Z_s over (Z_s+Z_r) or $7/40$. The simulations over these revolutions could provide a better frequency resolution or location. However, it was found that it was hard to determine which faulty characteristic frequency was the best choice as the magnitude difference in some fault frequency locations was quite effective while in some it was not that obvious. The residual signal, narrowband envelope, amplitude and phase demodulation analysis, and time-frequency analysis have been used in the subsequent analysis. From these analyses, it successfully indicated the number of faulted transient impacts involved within one carrier arm. For example, the faulted sun gear frequency is $N \frac{Z_r}{Z_s}$, as shown in equation (2) and the number of the faulted impacts should be $3 \times (99/21) \approx 14$. The residual signal in Fig. 10(b) and envelope signal in Fig. 11(b) as well as the amplitude and phase modulation analysis in Fig. 12(b) successfully reveal the number, which is 14. The interval between these sun gear faulted transient impacts should be equal between each other as it was induced by the faulted sun-planet mesh stiffness and therefore, the interval between two transient impacts is $7 \times 360/99 = 25.5^\circ$. The faulted planet gear frequency is $\frac{Z_r}{Z_p}$, as shown in equation (3) and the number of the faulted transient impacts should be $99/39 \approx 2.54$. The residual signal in Fig. 10(c) & (d) and the envelope signal in Fig. 11(c) & (d) as well as amplitude modulation analysis in Fig. 12(c) & (d) also successfully reveal the number, which is 3. Theoretically, the interval between these planet gear faulted transient impacts should be equal between each other and it should be $39 \times 360/99 = 141.8^\circ$ in this research as indicated by the mesh stiffness in table 2. However, as the planet gear tooth crack can happen either on the sun gear side or the ring gear side, the resultant gear mesh stiffness due to the crack can be quite different. Consequently, the resultant gear dynamic response was observed to be quite different if comparing Fig. 10(c) and Fig. 10(d) as well as Fig. 11(c) and Fig. 11(d). Similarly, the comparison can be made in Fig. 12(c) and Fig. 12(d). However, it should be mentioned here that the number of the faulted planet gear transient impacts is 2.54 and what has been presented and analysed in this research is the situation with 3 impacts within one carrier arm. There is also another situation when only 2 faulty planet gear impacts can be observed within one carrier arm, as shown in Fig. 14. This is largely because of the choice of the carrier arm revolution that acts as a window function, which is 360-deg wide while the interval between the faulty planet gear impacts is 141.8° . However, there is no problem for the faulty ring gear case as its interval between the faulty impacts is 120° , which means it will appear exactly three times within one carrier arm revolution. In another words, using the space between the impacts would be a powerful method to distinguish the fault on the planet gear and the fault on the ring gear. However, it does not matter if there would be two or three impacts, they are all caused by the same planet gear crack and they all indicate that there is crack on the planet gear. The faulted

ring gear frequency is N and the number of the faulted transient impacts is 3 as three planet gears pass the crack position one by one. The results in residual signal, envelope signal and amplitude modulation are seen in Fig. 10(e), Fig. 11(e), and Fig. 12(e) separately.

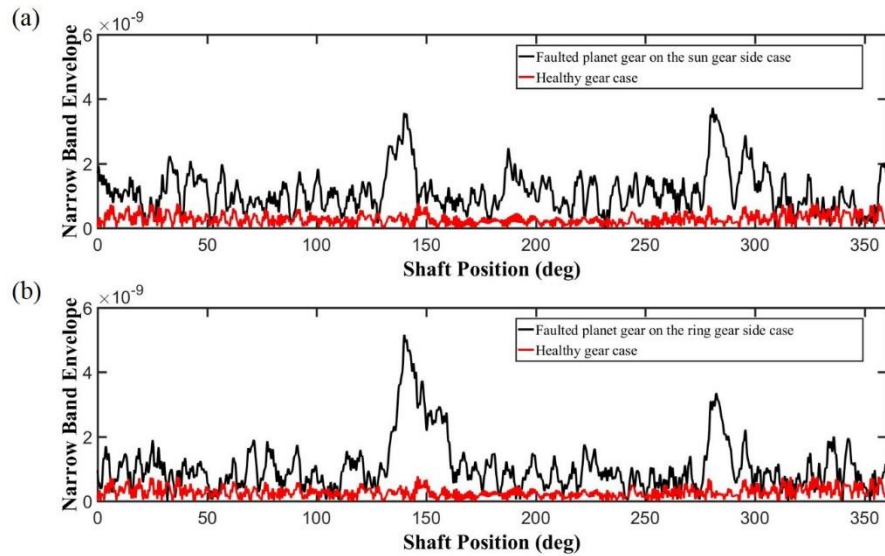


Figure 14 Faulty planet gear narrowband envelope results containing two impacts within one carrier arm revolution. (a) faulty planet gear on the sun gear side; (b) faulty planet gear on the ring gear side.

In the time-frequency domain, it was found that all the faults have similar behaviour to the faults on the fixed axis gear [34]. However, different energy distribution patterns were found in the presence of the localised tooth cracks for the sun gear, planet gear and ring gear. As pattern recognition [47] or image processing techniques [48] were often used to interpret the PWVD for detection of gear failure, it is expected to provide a more precise and easy to use method to identify the failure. Significant phase modulation and amplitude modulation, which was very similar to the results in [34], was found to occur when the crack was present in the simulation.

Limited planetary gear experimental work can be found in the published literatures, especially the condition monitoring using torsional vibration experimental work. Some early experimental work on this aspect was the work conducted at the Defence Science and Technology Organisation (DSTO) in Australia. Peter McFadden, David Forrester and Ian Howard investigated the vibration signal averaging of individual components in the planetary gearbox [3, 4]. In their report, a typical carrier arm signal was recorded with a damaged planet gear with 80% of one tooth removed. The amplitude modulation of the carrier arm signal clearly showed three fault impacts within one carrier arm revolution. The amplitude modulation results in Fig. 12(c)&(d) were compared with DSTO's data and they showed good agreement. Feng used extensive experimental work to valid his theoretical model. In his experimental results, the damaged sun gear, the damaged planet gear and the damaged ring gear were included and corresponding frequency spectra were analysed [11, 14]. The results in Fig. 8 can be seen to be in good agreement with Feng's work. All the faulty characteristic frequencies could be identified in the figure.

5. Conclusion

This paper has investigated the effectiveness of using torsional vibration signals as the diagnostic tool for the planetary gearbox fault detection. The lumped-parameter model was developed to obtain the dynamic response and the carrier arm torsional velocity was chosen to analysis the results. Gear faults on the sun gear, planet gear and ring gear were created using the finite element models and the corresponding resultant gear mesh stiffnesses were incorporated into the lumped-parameter model afterwards. The results of several diagnostic methods have been discussed in section 4. The RMS spectrum, residual signal, narrowband envelope, amplitude and phase demodulation analysis, and time-frequency analysis were used to analysis the torsional signals. It was found that the planetary gear torsional vibration was an effective alternative approach for the planetary gear condition monitoring. The narrowband envelope and the amplitude and phase demodulation were proven to be useful tools for analysing the planetary gear torsional vibration as they not only successfully revealed the presence of the fault, but also indicated the location of the fault. If the fault occurred on the sun gear, there were 14 transient impacts in the demodulation results while if the fault occurred on the planet gears, there were 2 or 3 transient impacts in the demodulation results. If the fault occurred on the ring gears, there were 3 transient impacts in the demodulation results. The space between these transient impacts was found to be an effective method to distinguish the fault position.

Acknowledgement

The funding support by Curtin University HDR Publication Scholarship is greatly acknowledged.

References

- [1] Inalpotat, M. (2009). *A theoretical and experimental investigation of modulation sidebands of planetary gear sets*. Ph. D Thesis, The Ohio State University, Colombia, United States.
- [2] Mark, W. D., & Hines, J. A. (2009). Stationary transducer response to planetary-gear vibration excitation with non-uniform planet loading. *Mechanical Systems and Signal Processing*, 23(4), 1366-1381.
- [3] Howard, I. M. (1991). *An investigation of vibration signal averaging of individual components in an epicyclic gearbox* (No. ARL-PROP-R-185). AERONAUTICAL RESEARCH LABS MELBOURNE (AUSTRALIA).
- [4] McFadden, P. D. (1991). A technique for calculating the time domain averages of the vibration of the individual planet gears and the sun gear in an epicyclic gearbox. *Journal of Sound and vibration*, 144(1), 163-172.
- [5] McFadden, P. D. (1994). Window functions for the calculation of the time domain averages of the vibration of the individual planet gears and sun gear in an epicyclic gearbox. *Journal of Vibration and Acoustics*, 116(2), 179-187.
- [6] McFadden, P. D., & Smith, J. D. (1985b). An explanation for the asymmetry of the modulation sidebands about the tooth meshing frequency in epicyclic gear vibration. *Proceedings of the Institution of Mechanical Engineers, Part C: Journal of Mechanical Engineering Science*, 199(1), 65-70.
- [7] McNames, J. (2002). Fourier series analysis of epicyclic gearbox vibration. *Journal of Vibration and Acoustics*, 124(1), 150-153.

- [8] Inalpolat, M., & Kahraman, A. (2009). A theoretical and experimental investigation of modulation sidebands of planetary gear sets. *Journal of Sound and Vibration*, 323(3), 677-696.
- [9] Inalpolat, M., & Kahraman, A. (2010). A dynamic model to predict modulation sidebands of a planetary gear set having manufacturing errors. *Journal of Sound and Vibration*, 329(4), 371-393.
- [10] Mark, W. D. (2009). Stationary transducer response to planetary-gear vibration excitation II: effects of torque modulations. *Mechanical Systems and Signal Processing*, 23(7), 2253-2259.
- [11] Feng, Z., & Zuo, M. J. (2012). Vibration signal models for fault diagnosis of planetary gearboxes. *Journal of Sound and Vibration*, 331(22), 4919-4939.
- [12] Randall, R. B. (2011). *Vibration-based condition monitoring: industrial, aerospace and automotive applications*. John Wiley & Sons.
- [13] Wang, Z. (2010). *Dynamic modelling of planetary gear systems for gear tooth fault*. Master Thesis, Curtin University, Perth, Australia.
- [14] Feng, Z., & Zuo, M. J. (2013). Fault diagnosis of planetary gearboxes via torsional vibration signal analysis. *Mechanical Systems and Signal Processing*, 36(2), 401-421.
- [15] Kahraman, A. (1994). Load sharing characteristics of planetary transmissions. *Mechanism and Machine Theory*, 29(8), 1151-1165.
- [16] Lin, J., & Parker, R. G. (1999). Sensitivity of planetary gear natural frequencies and vibration modes to model parameters. *Journal of Sound and Vibration*, 228(1), 109-128.
- [17] Velex, P., & Flamand, L. (1996). Dynamic response of planetary trains to mesh parametric excitations. *Journal of Mechanical Design*, 118(1), 7-14.
- [18] Gu, X., & Velex, P. (2012). A dynamic model to study the influence of planet position errors in planetary gears. *Journal of Sound and Vibration*, 331(20), 4554-4574.
- [19] Gu, X., & Velex, P. (2013). On the dynamic simulation of eccentricity errors in planetary gears. *Mechanism and Machine Theory*, 61, 14-29.
- [20] Chen, Z., & Shao, Y. (2013). Dynamic simulation of planetary gear with tooth root crack in ring gear. *Engineering Failure Analysis*, 31, 8-18.
- [21] Liang, X., Zuo, M. J., & Hoseini, M. R. (2015). Vibration signal modeling of a planetary gear set for tooth crack detection. *Engineering Failure Analysis*, 48, 185-200.
- [22] Xue, S., Entwistle, R., Mazhar, I., & Howard, I. (2016). The spur planetary gear torsional stiffness and its crack sensitivity under quasi-static conditions. *Engineering Failure Analysis*, 63, 106-120.
- [23] Ma, H., Pang, X., Feng, R., Song, R., & Wen, B. (2015). Fault features analysis of cracked gear considering the effects of the extended tooth contact. *Engineering Failure Analysis*, 48, 105-120.
- [24] Mohammed, O. D., Rantatalo, M., & Aidanpää, J. O. (2013). Improving mesh stiffness calculation of cracked gears for the purpose of vibration-based fault analysis. *Engineering Failure Analysis*, 34, 235-251.
- [25] Braun, S. (1975). The extraction of periodic waveforms by time domain averaging. *Acta Acustica united with Acustica*, 32(2), 69-77.
- [26] McFadden, P. D., & Smith, J. D. (1984). Vibration monitoring of rolling element bearings by the high-frequency resonance technique—a review. *Tribology international*, 17(1), 3-10.
- [27] McFadden, P. D. (1986). Detecting fatigue cracks in gears by amplitude and phase demodulation of the meshing vibration. *Journal of vibration, acoustics, stress, and reliability in design*, 108(2), 165-170.
- [28] McFadden, P. D. (1987). Examination of a technique for the early detection of failure in gears by signal processing of the time domain average of the meshing vibration. *Mechanical systems and signal processing*, 1(2), 173-183.

- [29] McFadden, P. D., & Smith, J. D. (1985). A signal processing technique for detecting local defects in a gear from the signal average of the vibration. *Proceedings of the Institution of Mechanical Engineers, Part C: Journal of Mechanical Engineering Science*, 199(4), 287-292.
- [30] Brie, D., Tomczak, M., Oehlmann, H., & Richard, A. (1997). Gear crack detection by adaptive amplitude and phase demodulation. *Mechanical Systems and Signal Processing*, 11(1), 149-167.
- [31] Meltzer, G., & Ivanov, Y. Y. (2003). Fault detection in gear drives with non-stationary rotational speed-part II: the time-quefrequency approach. *Mechanical Systems and Signal Processing*, 17(2), 273-283.
- [32] Forrester, B. D. (1996). *Advanced vibration analysis techniques for fault detection and diagnosis in geared transmission systems*. Ph.D Thesis, Swinburne University of Technology, Melbourne, Australia.
- [33] Wang, J., & Howard, I.M. (2004). The torsional stiffness of involute spur gears. *Proceedings of the Institution of Mechanical Engineers, Part C: Journal of Mechanical Engineering Science*, 218(1), 131-142.
- [34] Xue, S., & Howard, I. (2016). Dynamic modelling of flexibly supported gears using iterative convergence of tooth mesh stiffness. *Mechanical Systems and Signal Processing*, 80, 460-481.
- [35] Smith, J. D. (2003). *Gear noise and vibration*. CRC Press.
- [36] Wang, J. (2003). *Numerical and experimental analysis of spur gears in mesh*. Ph.D. Thesis, Curtin University, Perth, Australia.
- [37] Parker, R. G., & Lin, J. (2004). Mesh phasing relationships in planetary and epicyclic gears. *Journal of Mechanical Design*, 126(2), 365-370.
- [38] Liang, X., Zuo, M. J., & Pandey, M. (2014). Analytically evaluating the influence of crack on the mesh stiffness of a planetary gear set. *Mechanism and Machine Theory*, 76, 20-38.
- [39] Gomez, J. L., Bourdon, A., André, H., Rémond, D. (2016). Modelling deep groove ball bearing localized defects inducing instantaneous angular speed variations, *Tribology International*, 98, 270-281.
- [40] Li B., Zhang, X., Wu, J. (2017). New procedure for gear fault detection and diagnosis using instantaneous angular speed, *Mechanical Systems and Signal Processing*, 85, 415-428.
- [41] Rivola, A., Troncossi, M. (2014). Zebra tape identification for the instantaneous angular speed computation and angular resampling of motorbike valve train measurements, *Mechanical Systems and Signal Processing*, 44(1), 5-13.
- [42] Rémond, D., Antoni, J., Randall, R.B. (2014). Editorial for the special issue on Instantaneous Angular Speed (IAS) processing and angular applications, *Mechanical Systems and Signal Processing*, 44(1-2), 1-4.
- [43] Howard, I. M., Jia, S., & Wang, J. (2001). The dynamic modelling of a spur gear in mesh including friction and a crack. *Mechanical systems and signal processing*, 15(5), 831-853.
- [44] Howard, I. M. (1994). *A review of rolling element bearing vibration detection, diagnosis and prognosis*. (No. DSTO-RR-0013). DEFENCE SCIENCE AND TECHNOLOGY ORGANIZATION CANBERRA (AUSTRALIA).
- [45] Inalpolat, M., Handschuh, M., & Kahraman, A. (2015). Influence of indexing errors on dynamic response of spur gear pairs. *Mechanical Systems and Signal Processing*, 60, 391-405.
- [46] Mark, W. D., Reagor, C. P., & McPherson, D. R. (2007). Assessing the role of plastic deformation in gear-health monitoring by precision measurement of failed gears. *Mechanical systems and signal processing*, 21(1), 177-192.
- [47] Staszewski, W. J., Worden, K., & Tomlinson, G. R. (1997). Time-frequency analysis in gearbox fault detection using the Wigner-Ville distribution and pattern recognition. *Mechanical systems and signal processing*, 11(5), 673-692.

- [48] Wang, W. J. & McFadden, P. D. (1993b). Early detection of gear failure by vibration analysis—II. Interpretation of the time-frequency distribution using image processing techniques. *Mechanical System and Signal Processing*, 7(3), 205–215.

Appendix A

The following nomenclatures were used in this paper,

$I_m, I_s, I_{pi}, I_c, I_r, I_{out}$: mass inertia of the motor, sun gear, planet gear, carrier arm, ring gear, output load;

m_s, m_{pi}, m_c, m_r : mass of the sun, planet gear, carrier and ring;

$\theta_m, \theta_s, \theta_{pi}, \theta_c, \theta_r, \theta_{out}$: angular displacement of the motor, sun gear, planet gear, carrier arm, ring gear, output load;

x_j ($j = s, pi, c, r$): linear displacement in the horizontal direction measured in the rotating frame;

y_j ($j = s, pi, c, r$): linear displacement in the vertical direction measured in the rotating frame;

k_{cp}, k_{cg} : stiffness of the input coupling and shaft and the output coupling and shaft;

q_{cp}, q_{cg} : damping of the input coupling and shaft and the output coupling and shaft;

k_{sx}, k_{sy} : bearing radial stiffness of the sun gear;

q_{sx}, q_{sy} : bearing radial damping of the sun gear;

k_{rx}, k_{ry} : bearing radial stiffness of the ring gear;

q_{rx}, q_{ry} : bearing radial damping of the ring gear;

k_{cx}, k_{cy} : bearing radial stiffness of the carrier arm;

q_{cx}, q_{cy} : bearing damping of the carrier arm;

k_{pix}, k_{piy} : bearing stiffness of the planet gear;

q_{pix}, q_{piy} : bearing damping of the planet gear;

k_{spi}, k_{rpi} : mesh stiffness of the i -th sun-planet, ring-planet;

q_{spi}, q_{rpi} : mesh damping of the i -th sun-planet, ring-planet;

k_{rt}, q_{rt} : stiffness and damping of ring gear in the torsional direction;

r_s, r_p, r_r : base radius of the sun gear, planet gear, ring gear;

r_c : radius of the circle passing through planet gear centres;

T_{in}, T_{out} : input motor torque and output load torque;

$\delta_{spi}, \delta_{rpi}$: relative displacement on the lines of action of i -th sun-planet, ring-planet;

ϕ_i : circumferential angle of i -th planet;

Ω : carrier arm rotation speed;

f_m : the planetary gear tooth mesh frequency;

f_{sf}^e : the sun gear characteristic fault rotational frequency;

f_{pf}^e : the planet gear characteristic fault rotational frequency;

f_{rf}^e : the ring gear characteristic fault rotational frequency;

f_c : the carrier arm rotational frequency;

f_p : the planet gear rotational frequency;

f_s : the sun gear rotational frequency;

Appendix B

For the rotary motion of the motor, the differential equations are,

$$I_m \ddot{\theta}_m = T_{in} - T_s,$$

$$T_s = k_{cp}(\theta_m - \theta_s) + q_{cp}(\dot{\theta}_m - \dot{\theta}_s). \quad (1)$$

For the motion of the sun gear, the differential equations are,

$$m_s \ddot{x}_s + k_{sx} x_s + q_{sx} \dot{x}_s + \sum_{i=1}^3 [F_{spi} \cos(\varphi_{spi})] = m_s x_s \Omega^2 + 2m_s \dot{y}_s \Omega + m_s y_s \dot{\Omega},$$

$$m_s \ddot{y}_s + k_{sy} y_s + q_{sy} \dot{y}_s + \sum_{i=1}^3 [F_{spi} \sin(\varphi_{spi})] = m_s y_s \Omega^2 - 2m_s \dot{x}_s \Omega - m_s x_s \dot{\Omega},$$

$$(I_s/r_s) \ddot{\theta}_s + \sum_{i=1}^3 F_{spi} = T_s/r_s, \quad (2)$$

where F_{spi} is the normal contact force between the sun gear and the i th planet,

$$F_{spi} = k_{spi} \delta_{spi} + q_{spi} \dot{\delta}_{spi},$$

$$\delta_{spi} = (x_s - x_{pi}) \cos \varphi_{spi} + (y_s - y_{pi}) \sin \varphi_{spi} + r_s \theta_s + r_p \theta_{pi} - r_c \theta_c \cos \alpha_{sp},$$

$$\varphi_{spi} = \frac{\pi}{2} - \alpha_{sp} + \varphi_i,$$

$$\varphi_i = \frac{2\pi(i-1)}{3}; i = 1, 2, 3.$$

For the motion of the carrier arm, the differential equations are,

$$m_c \ddot{x}_c + k_{cx} x_c + q_{cx} \dot{x}_c - \sum_{i=1}^3 F_{cpix} = m_c x_c \Omega^2 + 2m_c \dot{y}_c \Omega + m_c y_c \dot{\Omega},$$

$$m_c \ddot{y}_c + k_{cy} y_c + q_{cy} \dot{y}_c + \sum_{i=1}^3 F_{cpiy} = m_c y_c \Omega^2 - 2m_c \dot{x}_c \Omega - m_c x_c \dot{\Omega},$$

$$(I_c/r_c) \ddot{\theta}_c + \sum_{i=1}^3 F_{cpix} \sin \varphi_i - \sum_{i=1}^3 F_{cpiy} \cos \varphi_i = T_c/r_c,$$

$$T_c = k_{cg}(\theta_c - \theta_{out}) + k_{cg} \cdot (\dot{\theta}_c - \dot{\theta}_{out}), \quad (3)$$

where F_{cpix} and F_{cpiy} describe the planet bearing forces between the carrier and the i -th planet in the x and y directions:

$$F_{cpix} = k_{pix}(x_{pi} - x_c) + q_{pix}(\dot{x}_{pi} - \dot{x}_c),$$

$$F_{cpiy} = k_{piy}(y_{pi} - y_c) + q_{piy}(\dot{y}_{pi} - \dot{y}_c).$$

For the motion of the planet gears:

$$\begin{aligned}
m_{pi}\ddot{x}_{pi} + F_{cpix} - F_{spi} \cos \varphi_{spi} - F_{rpi} \cos \varphi_{rpi} &= m_{pi}x_{pi}\Omega^2 + 2m_{pi}\dot{y}_{pi}\Omega + m_{pi}y_{pi}\dot{\Omega} + m_{pi}r_c\Omega^2 \cos \varphi_i, \\
m_{pi}\ddot{y}_{pi} + F_{cpiy} - F_{spi} \sin \varphi_{spi} - F_{rpi} \sin \varphi_{rpi} &= m_{pi}y_{pi}\Omega^2 - 2m_{pi}\dot{x}_{pi}\Omega - m_{pi}x_{pi}\dot{\Omega} + m_{pi}r_c\Omega^2 \sin \varphi_i, \\
(I_{pi}/r_p)\ddot{\theta}_{pi} + F_{spi} - F_{rpi} &= 0,
\end{aligned} \tag{4}$$

where F_{rpi} is the normal contact force between the ring gear and the i th planet,

$$\begin{aligned}
F_{rpi} &= k_{rpi}\delta_{rpi} + q_{rpi}\dot{\delta}_{rpi}, \\
\delta_{rpi} &= (x_r - x_{pi}) \cos \varphi_{rpi} + (y_r - y_{pi}) \sin \varphi_{rpi} + r_r\theta_r - r_p\theta_{pi} - r_c\theta_c \cos \alpha_{rp}, \\
\varphi_{rpi} &= \frac{\pi}{2} + \alpha_{rp} + \varphi_i,
\end{aligned}$$

For the motion of the ring gear, the motion equation is,

$$\begin{aligned}
m_r\ddot{x}_r + k_{rx}x_r + q_{rx}\dot{x}_r + \sum_{i=1}^3 F_{rpi} \cos \varphi_{rpi} &= m_rx_r\Omega^2 + 2m_r\dot{y}_r\Omega + m_ry_r\dot{\Omega}, \\
m_r\ddot{y}_r + k_{ry}y_r + q_{ry}\dot{y}_r + \sum_{i=1}^3 F_{rpi} \sin \varphi_{rpi} &= m_ry_r\Omega^2 - 2m_r\dot{x}_r\Omega - m_rx_r\dot{\Omega}, \\
(I_r/r_r)\ddot{\theta}_r + (q_{rt}/r_r)\dot{\theta}_r + (k_{rt}/r_r)\theta_r + \sum_{i=1}^3 F_{rpi} &= 0.
\end{aligned} \tag{5}$$

For the rotary motion of the load, the motion equation is,

$$I_{out}\ddot{\theta}_{out} = -T_{out} + T_c, \tag{6}$$

Appendix C

Physical parameters of a planetary gear set

	Sun gear	Planet gear	Ring gear	Carrier arm
Mass (Kg)	2.38	8.22	22.713	52
Mass inertia (Kg·m ²)	0.01	0.138	5.99	2.34
Bearing stiffness (N/m)	1×10 ⁵	1×10 ¹⁰	1×10 ¹⁰	1×10 ¹⁰
Bearing damping (Ns/m)	1×10 ³	1×10 ³	1×10 ³	1×10 ³